JEE Journal of Ecological Engineering

Journal of Ecological Engineering, 2026, 27(4), 163–176
https://doi.org/10.12911/22998993/214888
ISSN 2299–8993, License CC-BY 4.0

Received: 2025.11.13
Accepted: 2026.02.25
Published: 2026.03.10

Eco-friendly synthesis of $NiFe_2O_4$/ZnO composite for dual photocatalytic and antibacterial functions

Widia Purwaningrum[1,2*], Ady Mara[1], Muharni[1], Cingka Kurnia Rizki[1], Diyan Priani[1], Poedji Loekitowati Hariani[1,2]

[1] Department of Chemistry, Faculty of Mathematics and Natural Sciences, Universitas Sriwijaya, Jalan Palembang-Prabumulih, Indralaya, Ogan Ilir 30662, Indonesia
[2] Research Group on Magnetic Materials, Department of Chemistry, Faculty of Mathematics and Natural Sciences, Universitas Sriwijaya, Jalan Palembang-Prabumulih, Indralaya, Ogan Ilir 30662, Indonesia
* Corresponding author's e-mail: purwaningrum@mipa.unsri.ac.id

ABSTRACT

In this study, $NiFe_2O_4$/ZnO composites were biosynthesized using *Muntingia calabura* L. leaf extract and evaluated for Congo red dye photodegradation and antibacterial application. The material was characterized by X-ray diffraction (XRD), scanning electron microscope-energy dispersive X-Ray (SEM-EDX), ultraviolet–visible diffuse reflectance spectroscopy (UV-DRS), and vibrating sample magnetometry (VSM) analysis, confirming successful synthesis. Optimization process was performed using response surface methodology (RSM) with three variables: solution pH (4–10), dye concentration (10–40 mg/L), and irradiation time (30–90 minutes). The composite possessed a band gap energy of 2.23 eV along with magnetic characteristics, displaying a saturation magnetization of 42.89 emu/g. The crystallite size of the $NiFe_2O_4$/ZnO composite was determined to be 22.5 nm, confirming that this composite is on the nanoscale. The quadratic model ($R^2 = 0.9890$, $p < 0.05$) accurately described the degradation process, with optimum conditions at pH 6.20, dye concentration 38.10 mg/L, and irradiation time 52.30 minutes, achieving 98.10% degradation efficiency. A desirability value of 1 confirmed model validity, the predicted condition achieves the best outcome for all targeted responses simultaneously. The catalyst maintained stability during recycling, and antibacterial evaluation confirmed its effectiveness against *Staphylococcus aureus* and *Escherichia coli*. These findings highlight $NiFe_2O_4$/ZnO biosynthesized via *Muntingia calabura* L extract as an eco-friendly material with potential applications in wastewater treatment.

Keywords: green synthesis, $NiFe_2O_4$/ZnO, photocatalytic degradation, Congo red dye, RSM, antibacterial.

INTRODUCTION

Clean water is a fundamental necessity for life. However, population growth and rapid industrialization, which generate diverse types of waste, pose major challenges to securing water suitable for consumption (Adeleke et al., 2018; Liu et al., 2021). Among various pollutants, synthetic dyes remain a pressing concern. Dyes are extensively utilized in various industrial sectors, including textiles, paper, soap, plastics, paints, and cosmetics (Hitkari et al., 2022; Zhang et al., 2019). Azo dyes, in particular, account for approximately 80% of dyes used in textile manufacturing (Gaur et al., 2023). Their chemical structure is characterized by an azo group (–N=N–) that typically links aromatic rings such as benzene, naphthalene, or phenol. These dyes are valued for their vivid color stability, high solubility in water, and low cost. However, the discharge of wastewater rich in dyes leads to notable ecological and health hazards. Their resistance to natural degradation processes allows them to persist, disturbing aquatic life and threatening human well-being (Gadore et al., 2024; Gadow et al., 2022). Even at concentrations below 1 ppm, dyes can reduce light penetration in water bodies, thereby inhibiting photosynthesis in plants and plankton (Sarani et al., 2021). Congo red dye (CRD) is an azo dye. This dye is extremely poisonous and challenging

to decompose in the environment due to its complex molecular structure (Hitkari et al., 2022). This substance consists of benzidine derivatives, which may induce allergic reactions and, notably, can be converted into carcinogenic benzidine (Kannivelan & Rajappan, 2025).

ZnO is an n-type semiconductor widely employed as a photocatalyst (Kumar et al., 2025). It is favored for its high activity, mechanical and thermal stability, and environmental safety (Saad et al., 2020; Tijani et al., 2025). Despite these advantages, its photocatalytic efficiency remains limited since its wide band gap (3.37 eV) restricts absorption to UV radiation and the fast recombination of electron–hole pairs diminish activity (Mohan et al., 2024; Panchakeaw et al., 2025). These limitations hinder the practical application of ZnO as a photocatalyst. The synthesis of the $NiFe_2O_4$/ZnO composite entails integrating the p-type $NiFe_2O_4$ semiconductor with the n-type ZnO to establish heterojunctions has been shown to enhance photocatalytic performance by extending light absorption into the visible range, suppressing electron–hole recombination, and imparting magnetic properties that enable easy catalyst separation and recycling (Długosz et al., 2021; Makofane et al., 2022). In comparison to other ferrites, $NiFe_2O_4$ is particularly advantageous, as its spinel-type structure, remarkable chemical and mechanical stability, and narrow band gap (~1.9 eV) render it highly active under visible-light irradiation (Aggarwal et al., 2025; Chetia et al., 2024; Hemalatha et al., 2024).

Various methods are available for material synthesis, including sol-gel, co-precipitation, hydrothermal, electrochemical, sonochemical, and green synthesis approaches (Agarwal et al., 2025; Akbar et al., 2025). Among them, green synthesis is particularly attractive because it is environmentally friendly, simple, inexpensive, and non-toxic (Muhaymin et al., 2024). Plants, microorganisms, algae, enzymes, and fungi are natural resources that can function as reducing and stabilizing agents (Thirumavalavan et al., 2024). Several plant-based extracts have been successfully employed for the synthesis of $NiFe_2O_4$ and ZnO, including *Monsonia burkeana* (Makofane et al., 2022), *Hyphaene thebaica* fruit (Muhaymin et al., 2024), spent coffee extract (Winiarska et al., 2025), and *Justicia schemperiana* leaf extract (Yizengaw et al., 2025). In this study, $NiFe_2O_4$/ZnO was biosynthesized using *Muntingia calabura* L. leaf extract. This plant grows abundantly in tropical regions such as Thailand, Indonesia, Philippines and India. This plant is called kersen in Indonesia. The plant is often considered a wild species. Traditionally, the leaves of *Muntingia calabura* L. have been useds a hyperglycemic treatment and an antioxidant to prevent oxidative stress disorders (Taslim et al., 2023). The leaves contain abundant phenolics, terpenoids, and saponins that serve as natural bioreductants and stabilizing agents (Elviera et al., 2022; Sharma et al., 2025).

Previous studies have reported antibacterial properties of both ZnO and $NiFe_2O_4$. For instance, ZnO synthesized using *Jatropha curcas* latex extract exhibited activity against *Staphylococcus aureus*, *Bacillus subtilis*, and *Escherichia coli*, with greater inhibitory effects observed for green-synthesized ZnO compared to chemically synthesized counterparts (Sharma et al., 2025). Similarly, $NiFe_2O_4$ demonstrated activity against *Pseudomonas aeruginosa* and *Staphylococcus aureus* (Rincón-Granados et al., 2021).

In this study, a $NiFe_2O_4$/ZnO composite synthesised using *Muntingia calabura* L. leaf extract was applied for the photocatalytic degradation of CRD and antibacterial purposes. $NiFe_2O_4$/ZnO composite was examined through XRD, SEM-EDX, UV-DRS, and VSM techniques. Optimization of CRD degradation employing Response Surface Methodology. Furthermore, reusability assessments and antibacterial evaluations were performed against *Staphylococcus aureus (S. aureus)* and *Escherichia coli (E. coli)*. These findings suggest that $NiFe_2O_4$/ZnO offers multifunctional benefits as both a photocatalyst and an antibacterial agent.

MATERIALS AND METHODS

Materials

Muntingia calabura L. leaves were collected from Ogan Ilir Regency, South Sumatra, Indonesia. All chemicals used were of analytical grade, including $NiCl_2.6H_2O$ (≥98%), $FeCl_3.6H_2O$ (≥99%), NaOH (≥99%), and $Zn(NO_3)_2.6H_2O$ (≥98%), as well as Congo red dye (≥ 97%), Mueller–Hinton agar (MHA), Dimethyl sulfoxide (≥ 99.9%), and amoxicillin (96-99%) from Merck, Germany. The bacterial strains utilized were *S. aureus* (ATCC 25923) and *E. coli* (ATCC 25922). Throughout the study, distilled water was utilized as the solvent medium.

Muntingia calabura L. leaf extraction

The collected leaves were cleaned to remove impurities, rinsed thoroughly with distilled water and left to dry in air at room temperature for five days. The dried material was ground into a fine powder, from which 50 g was transferred into a 1 L Erlenmeyer flask. Subsequently, 500 mL of distilled water was added, and the flask was tightly sealed. The ratio between leaf powder and solvent (1:10). The mixture was left undisturbed for 24 h at room temperature before being filtered using Whatman filter paper, and the resulting aqueous extract was kept at 4 °C for later use (Adinarayana et al., 2024).

Synthesis of $NiFe_2O_4$

$NiCl_2.6H_2O$ (2.38 g) and $FeCl_3.6H_2O$ (5.41 g) were each dissolved in 12.5 mL of distilled water, then combined. To this mixture, 25 mL of *Muntingia calabura* L. leaf extract was introduced and stirred magnetically at 550 rpm for 120 min at room temperature. The pH of the solution was adjusted to 10 by the dropwise addition of 2 M NaOH in a closed vessel at room temperature. The resulting precipitate was washed repeatedly with distilled water until neutral (pH ~7), dried at 150 °C for 1 h, and finally calcined at 400 °C for 4 h (Hariani et al., 2025).

Synthesis of $NiFe_2O_4$/ZnO composite

The synthesis procedure was adapted from Pradhan et al., (2025). To synthesize the $NiFe_2O_4$/ZnO composite, 1 g of $NiFe_2O_4$ was first dispersed in a solution prepared by dissolving 3.56 g of $Zn(NO_3)_2 \cdot 6H_2O$ in 10 mL of distilled water (ratio mol $NiFe_2O_4$:ZnO = 0.004:0.04). This suspension was then mixed with 40 mL of *Muntingia calabura* L. leaf extract and stirred magnetically for 30 min at room temperature. The pH of the mixture was adjusted to approximately 10 by the gradual addition of 2 M NaOH in a closed vessel at room temperature. The precipitate obtained was thoroughly rinsed with distilled water until neutral conditions were reached, followed by drying at 150 °C for 1 h. Finally, the dried material was subjected to calcination at 400 °C for 4 h. A flowchart representation of the synthesis procedure is provided in Figure 1.

Material characterization

The obtained $NiFe_2O_4$ and $NiFe_2O_4$/ZnO composite materials were characterized using multiple techniques. Phase structure was analyzed using an X-ray diffraction (XRD, X'Pert PRO) over a 2θ range of 10–90° (CuKα = 1.54056 Å, 40/30 kV/mA, at 2°/min). Optical properties were determined by ultraviolet–visible diffuse reflectance spectroscopy (UV-DRS, Cary 60, version 2.00) in the wavelength range of 200–900 nm. Morphology and elemental distribution were examined using a scanning electron microscope-energy dispersive X-ray spectroscopy (SEM-EDX, Hitachi FlexSEM 100). Analyses were performed using an accelerating voltage of 20 kV, a 60-second counting time, and a probe current of 45 nA. Magnetic characteristics were measured with a vibrating sample magnetometer (VSM, Oxford Type 1.2 T). The analysis was carried out at room temperature with a field range of −10 to +10 kOe, a vibration frequency of 80 Hz, and an amplitude of 1.5 mm. Dye absorbance was measured with a UV–Vis spectrophotometer (Orion Aquamate 8000).

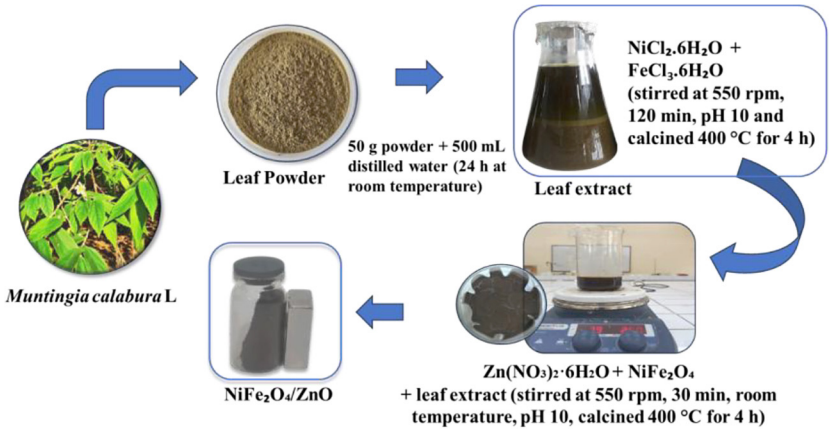

Figure 1. Schematic diagram of green synthesis of $NiFe_2O_4$/ZnO composite

Photocatalytic experiment

Three independent variables: pH (4–10), dye concentration (10–40 mg/L), and irradiation time (30–90 minutes) were selected to evaluate the performance of $NiFe_2O_4$/ZnO as a catalyst in dye degradation. Each experiment used 0.05 g of $NiFe_2O_4$/ZnO in 100 mL of dye solution. A 200 W xenon lamp served as the light source, with the sample solution positioned 20 cm from the lamp. To achieve adsorption equilibrium, the mixture was stirred for 30 minutes in the dark at room temperature. The interactions between the variables were analyzed using response surface methodology (RSM) with a central composite design (CCD) to determine the optimum degradation conditions. Experimental design and statistical analysis were conducted using Design Expert software version 13. A total of 20 experimental runs were performed, each in triplicate. The concentration of CRD was determined by measuring its absorbance using a UV-Vis spectrophotometer, and the degradation efficiency was calculated using the following equation.

$$Degradation\ (\%) = \frac{C_0 - C_i}{C_0} \times 100\ \% \quad (1)$$

where: C_0 and C_i are the initial concentration and final concentration after degradation (mg/L)

Antibacterial activity

Antibacterial activity was evaluated using a modified agar diffusion method (Atiek et al., 2024), with *S. aureus* and *E. coli* as test organisms. Dimethyl sulfoxide (DMSO) and amoxicillin were employed as negative and positive controls, respectively. Mueller–Hinton Agar (MHA) was used as the culture medium, while bacterial inocula were prepared by growing each strain in Mueller–Hinton Broth (MHB) at 37 °C for 24 h and adjusting the suspension to a turbidity of 0.5 McFarland. For stock preparation, 500 mg of catalyst was suspended in 50 mL of DMSO to achieve a concentration of 10 mg/mL. From this, five working concentrations (5000, 4000, 3000, 2000, and 1000 µg/mL) were prepared. Sterile 6 mm paper discs were immersed in ~1 mL of each sample solution until saturated and then placed on the surface of MHA plates previously inoculated with bacterial suspension using a sterile cotton swab. The plates were incubated in an inverted position at 37 °C for 24–36 h. After incubation, inhibition zones were observed around each disc, and their diameters were measured. Each experiment was conducted three times.

RESULTS AND DISCUSSION

$NiFe_2O_4$/ZnO characterization

The XRD spectra of $NiFe_2O_4$ and $NiFe_2O_4$/ZnO are shown in Figure 2. The diffraction peaks of $NiFe_2O_4$ are consistent with JCPDS No. 10-0325, appearing at 2θ = 30.51°, 35.81°, 43.34°, 53.92°, 57.49°, and 62.94°, corresponding to the (220), (311), (400), (422), (511), and (440) planes, respectively, with a cubic spinel structure. The sharp peak at 2θ = 35.81°, assigned to the (311) plane, is the main characteristic reflection of $NiFe_2O_4$.

For $NiFe_2O_4$/ZnO, the diffraction pattern shows a combination of $NiFe_2O_4$ and ZnO peaks, confirming the coexistence of two phases. The intensity of the peaks depends on the relative ratio of both components. ZnO peaks were observed at 2θ = 31.79°, 34.43°, 36.24°, 47.65°, 56.77°, 62.97°, 67.90°, and 69.21°, which correspond to the (100), (002), (101), (102), (110), (103), (112), and (201) planes, consistent with JCPDS No. 89-0510. ZnO crystallizes in the hexagonal wurtzite structure, where Zn^{2+} and O^{2-} atoms are tetrahedrally coordinated (Roy et al., 2022). The sharp reflection at 2θ = 34.43° indicates high ZnO crystallinity. The coexistence of both $NiFe_2O_4$ and ZnO reflections further validates the successful synthesis of the $NiFe_2O_4$/ZnO composite (Majeed et al., 2024).

The crystallite sizes were estimated using the Debye–Scherrer equation, yielding 16.2 nm for $NiFe_2O_4$ and 22.9 nm for $NiFe_2O_4$/ZnO within the nanoscale range. The crystallite size has a critical influence on the photocatalytic process. The smaller crystallite size favors the formation of $NiFe_2O_4$/ZnO heterojunctions. This structural feature is beneficial for photocatalysis, as smaller crystallite sizes provide a larger active surface area, while the heterojunctions promote more efficient wiring and transfer of photogenerated charge carriers. The smaller crystallites contribute to improved lattice organization and band gap narrowing, which together favor higher photodegradation activity (Makofane et al., 2022). Moreover, the XRD results confirmed that the use of *Muntingia calabura* L. leaf extract as a green

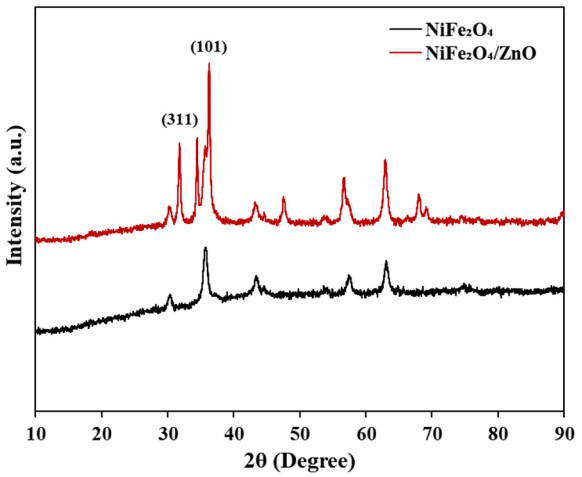

Figure 2. Spectra XRD of $NiFe_2O_4$ and $NiFe_2O_4$/ZnO composite

synthesis agent did not alter the crystal structure, as no significant 2θ shift was observed.

As shown in Figure 3, $NiFe_2O_4$ demonstrates non-uniform particle dimensions with a marked tendency toward agglomeration. This agrees with prior studies, where coprecipitation-derived $NiFe_2O_4$ generally presents comparable morphological characteristics (Shokri et al., 2023). The aggregation is mainly attributed to the high surface energy of nanoparticles, which drives them to minimize energy by clustering. Additionally, Van der Waals forces further promote particle attraction and agglomeration. In contrast, the $NiFe_2O_4$/ZnO composite shows a more homogeneous and compact morphology with relatively uniform grain sizes. The incorporation of ZnO appears to restrict the excessive growth of $NiFe_2O_4$ crystallites, as Fe_3O_4 particles are dispersed at the ZnO interface. This interaction effectively limits grain coarsening and reduces agglomeration, leading to improved particle distribution.

Elemental mapping verified the presence of O, Ni, Fe, and Zn, with corresponding weight percentages of 32.46%, 7.10%, 16.32%, and 44.12%. The absence of impurity elements validates the successful synthesis of the $NiFe_2O_4$/ZnO composite. The carbon element in the *Muntingia calabura* L leaf extract is likely lost during calcination.

The UV–DRS spectra of $NiFe_2O_4$ display a broad absorption band extending into the visible light region (~700 nm), consistent with its narrow band gap of 1.91 eV as determined from the Tauc

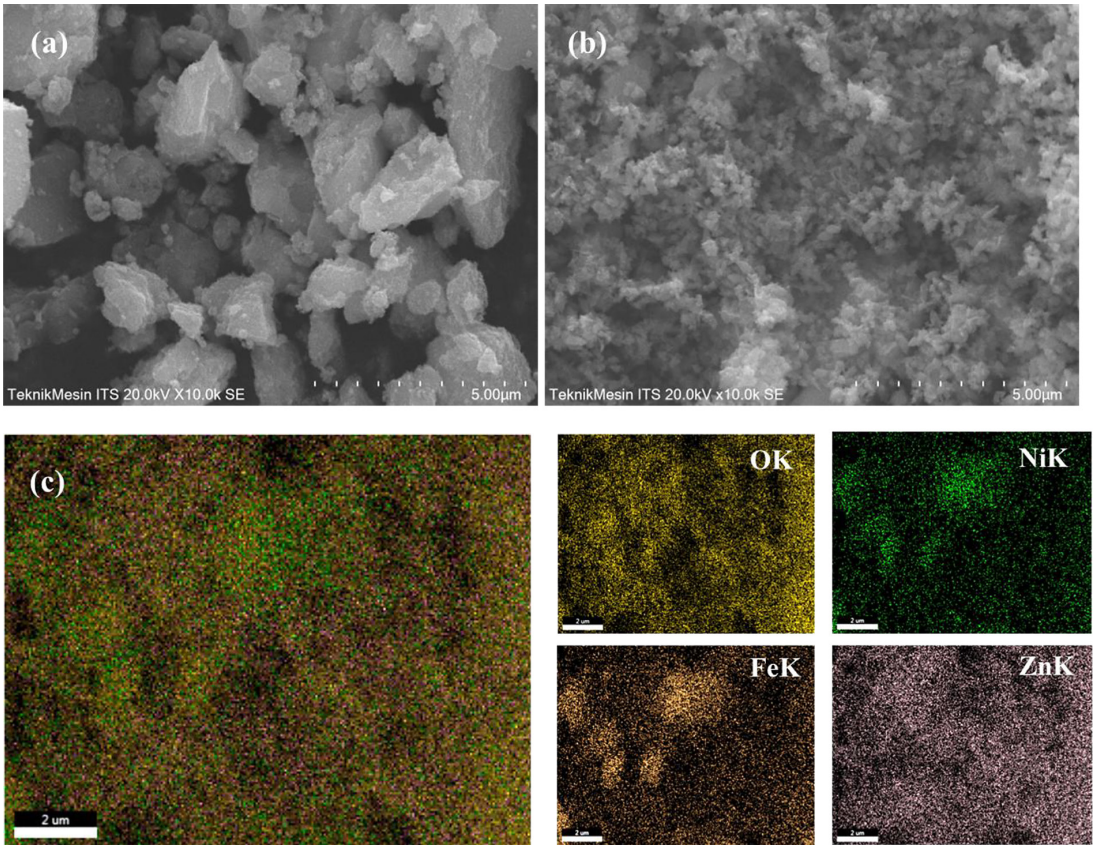

Figure 3. SEM image of of (a) $NiFe_2O_4$, (b) $NiFe_2O_4$/ZnO composite and (c) elemental mapping of $NiFe_2O_4$/ZnO composite

plot. While pure ZnO suffers from limited visible-light utilization due to its band gap exceeding 3.0 eV, the incorporation of $NiFe_2O_4$ reduces this limitation. The resulting $NiFe_2O_4$/ZnO system displays an absorption edge at approximately 379 nm, indicating a band gap energy of 2.23 eV (Fig. 4). The observed blue shift compared with pure $NiFe_2O_4$ suggests the formation of a heterojunction between $NiFe_2O_4$ and ZnO. Such interfacial interactions facilitate charge transfer, reduce electron–hole recombination, and broaden the optical absorption window, enabling activity not only in the UV but also across the visible region. Another study showed that the $NiFe_2O_4$/ZnO produced by the coprecipitation method had a band gap value of 2.5 eV (Tripta & Rana, 2023). These findings confirm that the $NiFe_2O_4$/ZnO not only maintains the visible-light activity of $NiFe_2O_4$ but also improves the overall photocatalytic potential by synergistically combining the optical properties of both components.

The hysteresis behavior of $NiFe_2O_4$ and $NiFe_2O_4$/ZnO was characterized by VSM across the magnetic field range of –10,000 to +10,000 Oe (Fig. 5). For pure $NiFe_2O_4$, the saturation magnetization (Ms) was determined to be 49.06 emu/g. This relatively high value arises because the magnetic moments of Ni^{2+} and Fe^{3+} ions located at tetrahedral and octahedral sites do not completely cancel each other out. Bulk $NiFe_2O_4$ typically exhibits Ms values in the range of 50–65 emu/g, and the value obtained in this study falls within this range. Interestingly, it is also substantially higher than the Ms of $NiFe_2O_4$ synthesized using *Terminalia chebula* fruit extract (16.34 emu/g) as reported by Aggarwal et al., (2025).

$NiFe_2O_4$ incorporation with ZnO, the Ms value decreased to 42.89 emu/g. This reduction can be attributed to the dilution effect of the non-magnetic ZnO phase, which restricts the motion of magnetic domains and thereby lowers the overall magnetization. Nevertheless, the composite still exhibits a sufficiently high Ms value, which enables its use in magnetically assisted separation and related applications. $NiFe_2O_4$ typically exhibits coercivity in the range of 20–200 Oe and remanent magnetization (Mr) of 0.5–10 emu/g, while ZnO is non-magnetic (Hc ≈ 0; Mr ≈ 0). Therefore, the composite is expected to maintain soft magnetic behavior. $NiFe_2O_4$/ZnO can be separated from the solution in a comparatively short time (30–120 seconds).

Photocatalytic performance

The effect of pH (A), dye concentration (B), and irradiation time (C) on CRD degradation was examined using RSM. A CCD consisting of 20 runs was adopted (Table 1). The Analysis of variance (ANOVA) results indicated that a quadratic model provided the best description of the correlation between the variables and the degradation efficiency. This model incorporates both linear and interaction terms, with coefficients reflecting positive or negative contributions to the response. The estimated degradation efficiency was represented by the following quadratic equation.

$$\begin{aligned}\text{Degradation (\%)} = {} & -70.65141 + 15.61419A \\ & + 3.23382B + 2.20429C - 0.075444AB \\ & + 0.063000AC - 0.015933BC - 1.28843A^2 \\ & - 0.026160B^2 - 0.018245C^2\end{aligned} \quad (2)$$

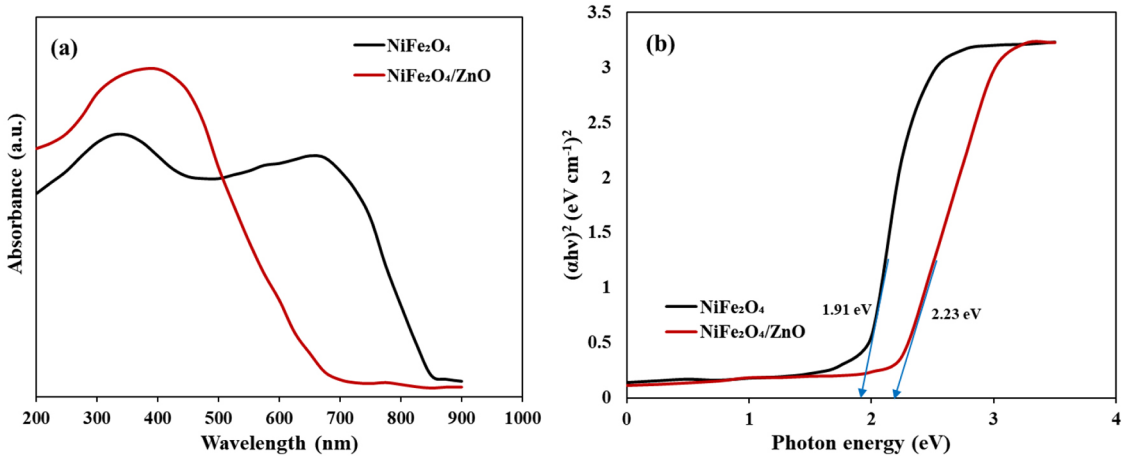

Figure 4. (a) UV-DRS results and (b) band gap plots of $NiFe_2O_4$ and $NiFe_2O_4$/ZnO composite

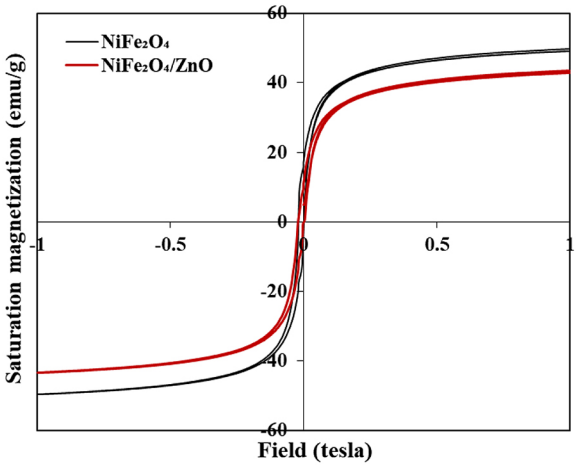

Figure 5. Hysteresis curves of $NiFe_2O_4$ and $NiFe_2O_4$/ZnO composite

Figure 6 shows a plot between the actual (experimental) and predicted values. The graph shows that the points approach a straight line, with no points deviating significantly. The residual error range between the experimental and predicted results ranges from 0.022 to 3.10. Therefore, the prediction model is very good because the predicted values are nearly identical to the actual values.

Independent variables with a p-value < 0.05 and a high F-value are considered statistically significant (Mohammadi et al., 2024). As presented in Table 2, pH, dye concentration, and irradiation time each showed p-values < 0.05, confirming their significant influence on the degradation efficiency. The model achieved an R^2 value of 0.9890, demonstrating that 98.90% of the variability in the response was accounted for by the model, while only 1.10% was attributed to other factors or experimental error.

Furthermore, the difference between the adjusted R^2 and predicted R^2 values was small (0.0685), well below the threshold of 0.2, which suggests strong model reliability and the absence of overfitting (Boucherdoud et al., 2025). The Adeq Precision value was greater than 4, further supporting that the model provides an adequate signal-to-noise ratio and can be reliably used for prediction.

Interactions between variables

3D response surfaces along with 2D contour plots were constructed to demonstrate how pH, dye concentration, and irradiation time

Table 1. Comparison of the actual and predicted value of degradation efficiency

Run	pH	CRD concentration (mg/L)	Irradiation time (min)	Response (%)		Residual
				Actual	Predicted	
1	10	40	30	63.23	63.46	-0.23
2	4	40	90	62.11	62.54	-0.43
3	10	10	90	69.61	71.79	-2.18
4	7	25	60	97.8	95.95	1.85
5	7	25	60	97.61	95.95	1.66
6	4	40	30	87.11	84.76	2.35
7	4	10	90	57.23	56.84	0.39
8	7	25	60	95.34	95.94	-0.60
9	10	40	90	65.68	63.91	1.77
10	7	25	60	96.81	95.94	0.87
11	7	25	90	81.67	81.25	0.42
12	7	25	60	92.84	95.94	-3.10
13	7	25	60	97.34	95.94	1.40
14	10	10	30	43.25	42.65	0.60
15	4	25	60	85.22	85.94	-0.72
16	4	10	30	48.78	50.38	-1.60
17	10	25	60	82.78	82.76	0.02
18	7	10	60	86.21	83.43	2.78
19	7	25	30	76.68	77.79	-1.11
20	7	40	60	94.21	96.68	-2.47

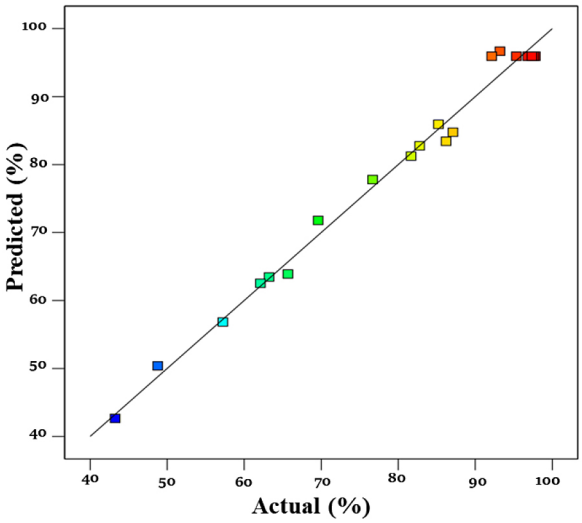

Figure 6. Predicted versus actual diagram

interactively affect photodegradation efficiency (Fig. 7). In both plots, the red regions indicate the optimum conditions for CRD degradation. The results show that degradation efficiency initially increases with higher concentration and pH, but beyond a certain point begins to decline. Consistent results were obtained for interactions involving pH with irradiation time and dye concentration with irradiation time.

Experimentally, the optimum conditions were achieved at pH 7, dye concentration of 40 mg/L, and irradiation time of 60 minutes, yielding a degradation efficiency of 96.68%. According to the quadratic model, the predicted optimum conditions were pH 6.20, dye concentration 38.10 mg/L, and irradiation time 52.30 minutes, with a degradation efficiency of 98.10% and a desirability value of 1. The desirability value of 1 confirms the validity of the model, demonstrating excellent agreement between the experimental results and the model predictions (Hasanpour et al., 2021).

The photocatalytic degradation process initiates through an electrostatic interaction between the dye molecules and the catalyst surface. CRD is an anionic dye (negatively charged) containing a sulfonate group ($–SO_3^-$), while the catalyst surface is generally positively charged. The efficiency of hydroxyl radical (•OH) and superoxide radical ($O_2•^-$) formation is strongly influenced by pH. At too low a pH, the formation of hydroxyl radicals is suppressed, whereas at highly basic pH, these radicals may become deactivated. The $NiFe_2O_4$/ZnO composite has a pHpzc of 7.3 (Fig. 8). CRD is an anionic dye that increases the electrostatic interaction between negatively charged molecules and the positive surfaces of the $NiFe_2O_4$/ZnO composite. Moreover, at high pH values, repulsion occurs between the dye and the catalyst surface, since both carry negative charges (Khera & Jeevanandam, 2025; Riyanti et al., 2025).

These observations are consistent with previous studies reporting that the photocatalytic

Table 2. ANOVA summary of CRD degradation

Description	Sum of squares	Df	Mean square	F-value	p-value	
Model	5580.44	9	620.05	99.79	< 0.0001	significant
A-pH	25.28	1	25.28	4.07	0.0473	
B-Concentration	439.04	1	439.04	70.66	< 0.0001	
C-Irradiation	29.76	1	29.76	4.79	0.0535	
AB	92.21	1	92.21	14.84	0.0032	
AC	257.19	1	257.19	41.39	< 0.0001	
BC	411.27	1	411.27	66.19	< 0.0001	
A^2	369.78	1	369.78	59.51	< 0.0001	
B^2	95.27	1	95.27	15.33	0.0029	
C^2	741.53	1	741.53	119.34	< 0.0001	
Residual	62.13	10	6.21			
Lack of Fit	38.72	5	7.74	1.65	0.2971	not significant
Pure Error	23.41	5	4.68			
Cor Total	5642.58	19				
Fit Statistic						
Std Dev	R^2		Adj R^2	Pred R^2	Adeq Prec.	C.V.%
2.49	0.9890		0.9791	0.9106	30.6530	3.16

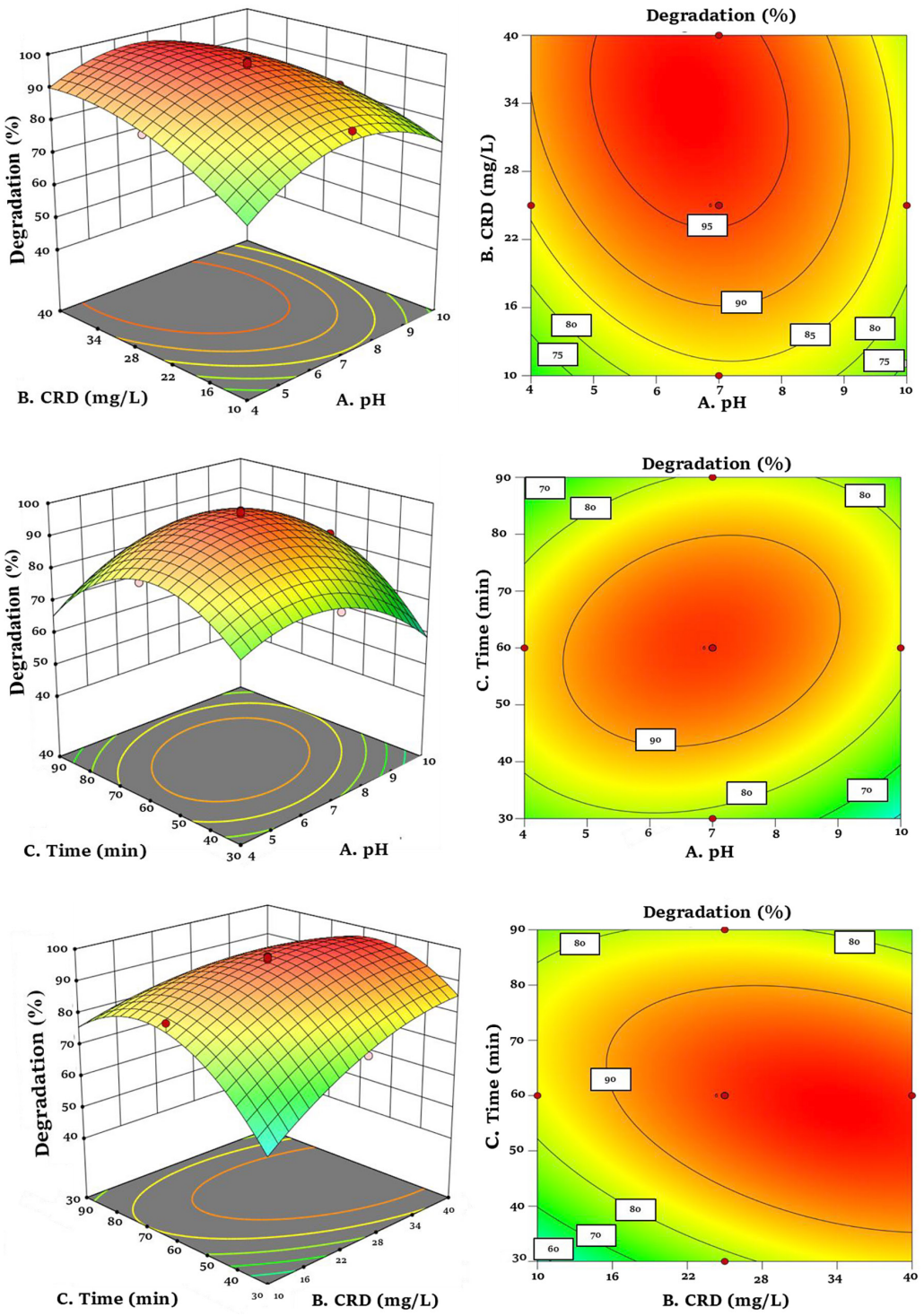

Figure 7. 3D response surface and 2D contours of photocatalytic degradation of CRD

degradation of CRD is most effective within the pH range of 6–7 (Boucherdoud et al., 2025; Sarkar et al., 2021). At low dye concentrations, the molecules are easily adsorbed onto the catalyst surface, while UV/Vis light can also penetrate efficiently to activate the catalyst. Under these conditions, the radicals (•OH, $O_2^{\bullet-}$) formed are sufficient to attack and degrade the dye molecules. Conversely, at very high concentrations, photons are unable to effectively reach the catalyst surface because they are absorbed or blocked by the dense dye layer (Riyanti et al., 2025).

The irradiation time also plays a critical role. Longer exposure generates more Reactive Oxygen Species (ROS), thereby enhancing degradation. However, once the optimum conditions are

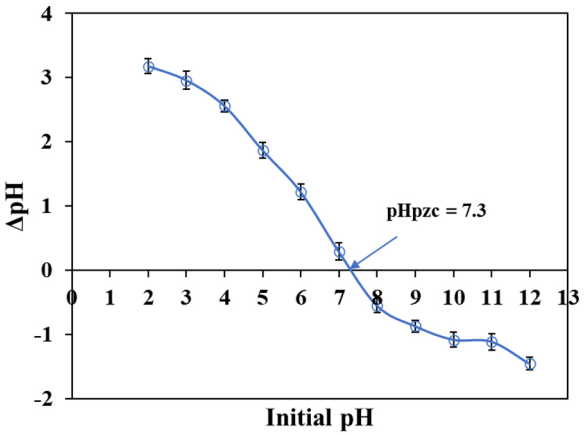

Figure 8. pHpzc of $NiFe_2O_4$/ZnO composite

reached, extending irradiation time does not significantly improve yield, since most CRD molecules have already degraded and the degradation rate naturally decreases.

The degradation mechanism that occurs can be explained as follows (Khan et al., 2023; Sofia et al., 2025).

$$NiFe_2O_4/ZnO + h\nu \rightarrow \rightarrow NiFe_2O_4/ZnO\ (e_{CB}^- + h_{VB}^+) \quad (3)$$

$$e_{CB}^- + O_2 \rightarrow O_2^{\bullet -} \quad (4)$$

$$h_{VB}^+ + H_2O \rightarrow {}^{\bullet}OH + H^+ \quad (5)$$

$$CRD + {}^{\bullet}OH \rightarrow CO_2 + H_2O \quad (6)$$

$$CRD + O_2^{\bullet -} \rightarrow CO_2 + H_2O + \text{other product} \quad (7)$$

Reusability of catalyst

Catalyst recycling is essential for evaluating sustainability from both environmental and economic perspectives, particularly for industrial applications. Industries favor catalysts with long lifetimes because they are more cost-effective, easier to handle, and minimize replacement frequency. In this study, recycling and retesting were conducted under the optimum conditions of pH 6.20, dye concentration 38.10 mg/L, and irradiation time 52.30 minutes. Post-cycle, the catalyst underwent centrifugation recovery, distilled water washing, and overnight drying at room temperature inside a vacuum desiccator (Khera & Jeevanandam, 2025).

The degradation efficiency was 98.10% in the first cycle and gradually decreased to 97.54%, 95.60%, 94.80%, and 93.46% over subsequent cycles (Fig. 9). Thus, the overall decline of 4.64% after five cycles is considerably smaller than reported for other systems, such as CuO_2@PANI, which showed a drop from 85.4% to 80.3% after only four cycles (Boucherdoud et al., 2025). The observed reduction in performance can be attributed to partial loss of catalyst during recovery and the adhesion of dye molecules or degradation products to the catalyst surface.

Antibacterial activity

The antibacterial properties of $NiFe_2O_4$/ZnO composite were investigated via the disk-diffusion method against Gram-positive (*S. aureus*) and Gram-negative (*E. coli*) strains. The bactericidal effectiveness of materials depends on several physicochemical factors, including Reactive Oxygen Species (ROS) generation, surface area, particle size, solubility, and surface charge (Chan et al., 2024). ROS are particularly crucial, as they compromise the integrity of bacterial membranes and induce damage to DNA and proteins, leading to cell death. Furthermore, interactions involving metal ion deposition on bacterial cells can interfere with normal physiology and enhance antimicrobial potency (Sofia et al., 2025).

As shown in Table 3, increasing the concentration of $NiFe_2O_4$/ZnO produced larger inhibition zones. DMSO served as the negative control and showed no inhibition zone, while amoxicillin (positive control) produced a zone of 24.6 and 22.4 mm. $NiFe_2O_4$/ZnO exhibited stronger

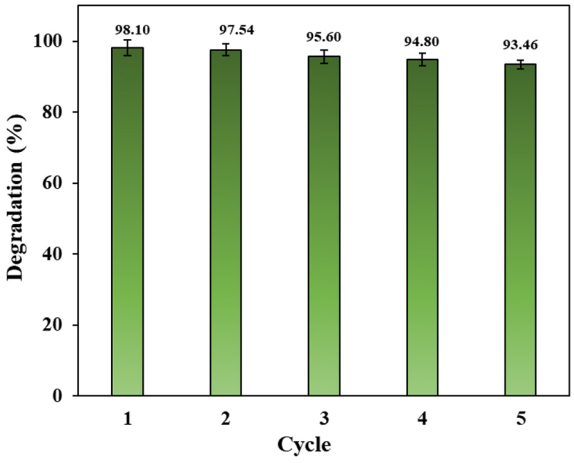

Figure 9. The degradation efficiency of $NiFe_2O_4$/ZnO composite for 5 cycles

Table 3. Zone of inhibition of $NiFe_2O_4$/ZnO composite

Concentration (µg/mL)	Zone of Inhibitions (mm)	
	S. aureus	*E. coli*
1000	8.6 ± 0.5	8.1 ± 0.4
2000	11.2 ± 0.7	9.8 ± 0.6
3000	14.6 ± 0.5	11.2 ± 0.9
4000	16.2 ± 0.6	14.3 ± 0.8
5000	17.3 ± 0.9	16.5 ± 1.0
Amoxicillin (+)	24.6 ± 1.1	22.4 ± 0.9
DMSO (-)	0	0

inhibition against *S. aureus* than *E. coli* across all concentrations. Similar results have been reported for $NiFe_2O_4$ synthesized from lime peel extract (Malik et al., 2022) and ZnO derived from *Jatropha curcas* latex (Sharma et al., 2025). The higher susceptibility of *S. aureus* is attributed to its thick peptidoglycan cell wall lacking an outer membrane, which makes it more prone to membrane damage and leakage of cellular contents (Rincón-Granados et al., 2021; Shokri et al., 2023). The antibacterial activity of $NiFe_2O_4$/ZnO is not intended to replace pharmaceutical antibiotics, but rather functions as an agent that inhibits bacterial growth in the environment. Its ability to suppress the proliferation of bacteria such as *S. aureus* and *E. coli* is still lower than the effectiveness of commercial antibiotics. However, $NiFe_2O_4$/ZnO composite potentially being used as a supporting material in wastewater treatment.

CONCLUSIONS

$NiFe_2O_4$/ZnO composites were successfully biosynthesized using *Muntingia calabura* L. leaf extract as a bioreductant and stabilizing agent. Structural and optical characterization (XRD, SEM-EDX, UV-DRS, and VSM) confirmed the successful formation of the catalyst, with a band gap of 2.23 eV, indicating visible-light activity. RSM-based ANOVA analysis demonstrated that a quadratic model reliably described the photocatalytic degradation of Congo red dye, with optimum conditions at pH 6.20, dye concentration 38.10 mg/L, and irradiation time 52.30 minutes, achieving 98.10% degradation efficiency. The catalyst exhibited excellent stability, exhibiting a mere 4.64% drop in efficiency after five consecutive reuse cycles, and its magnetic properties enabled easy recovery and recycling. Furthermore, $NiFe_2O_4$/ZnO showed strong antibacterial activity, with greater inhibition against *S. aureus* than *E. coli*. Overall, the combination of efficient photocatalytic activity, high reusability, antibacterial potential, and green synthesis highlights $NiFe_2O_4$/ZnO composite as a promising material for future environmentally friendly wastewater treatment applications.

Acknowledgments

Funding for this research was obtained through the Directorate of Research and Community Service, Directorate General of Research and Development, Ministry of Higher Education, Science, and Technology, under the 2025 Fundamental Research scheme of the State University Operational Assistance Program (Contract No. 109/C3/DT.05.00/PL/2025).

REFERENCES

1. Adeleke, J. T., Theivasanthi, T., Thiruppathi, M., Swaminathan, M., Akomolafe, T., & Alabi, A. B. (2018). Photocatalytic degradation of methylene blue by ZnO/$NiFe_2O_4$ nanoparticles. *Applied Surface Science*, *455*, 195–200. https://doi.org/10.1016/j.apsusc.2018.05.184
2. Adinarayana, D., Annapurna, N., Mohan, B. S., & Douglas, P. (2024). Enhanced photocatalytic removal of Cr(VI) and Rhodamine B from water using plant-mediated CdS nanoparticles: Mechanistic insights and environmental applications. *Desalination and Water Treatment*, *320*. https://doi.org/10.1016/j.dwt.2024.100593
3. Agarwal, B., Rani, M., & Shanker, U. (2025). Green biosynthesized $NiFe_2O_4$ coated with rGO for efficient photocatalytic degradation of plastic additives: Synthesis, mechanism, and kinetics. *Diamond and Related Materials*, *153*. https://doi.org/10.1016/j.diamond.2025.112115
4. Aggarwal, D., Bhavika, Kaur, M., Bansal, S., & Singhal, S. (2025). Fabrication of eco-friendly $NiFe_2O_4$ nanocatalysts via plant extract-mediated synthesis: Kinetic and mechanistic insights into photocatalytic degradation of an anthraquinone dye and tetracycline antibiotic. *Journal of Molecular Structure*, *1319*, 139365. https://doi.org/10.1016/j.molstruc.2024.139365
5. Akbar, A., Bhavani Lakshmi, M., Das, T. K., & Ghosh, M. (2025). Spinel ferrites in the photocatalytic and adsorptive remediation of dyes and heavy metals: A review. In *Journal of Water Process Engineering, 71*, 107259. https://doi.org/10.1016/j.jwpe.2025.107259

6. Atiek, E., Matebu, A., Tsegaye, D., Behailu, G., & Abebe, B. (2024). Green synthesis of TiO_2/ZnO heterostructure using Urtica Smensis leaf extract for antibacterial activity. *Results in Chemistry*, *12*, 101880. https://doi.org/10.1016/j.rechem.2024.101880
7. Boucherdoud, A., Seghier, A., Kherroub, D. E., Douinat, O., Dahmani, K., Bestani, B., & Benderdouche, N. (2025). Autogenous deposition of copper oxide onto polyaniline nanocomposite catalysts for the photodegradation of Methylene blue and Congo red: Experimental inquiry, RSM optimization, and DFT calculation. *Materials Science and Engineering: B*, *314,* 118015. https://doi.org/10.1016/j.mseb.2025.118015
8. Chan, Y. Bin, Aminuzzaman, M., Rahman, M. K., Win, Y. F., Sultana, S., Cheah, S. Y., Watanabe, A., Wong, L. S., Guha, S. K., Djearamane, S., Rajendran, V., Akhtaruzzaman, M., & Tey, L. H. (2024). Green synthesis of ZnO nanoparticles using the mangosteen (Garcinia mangostana L.) leaf extract: Comparative preliminary in vitro antibacterial study. *Green Processing and Synthesis*, *13*(1), 20230251. https://doi.org/10.1515/gps-2023-0251
9. Chetia, T., Suleman, A., & Chetia, B. (2024). A comprehensive review on magnetic $NiFe_2O_4$ nanoparticles: Synthesis approaches and catalytic proficiency in various coupling reactions. *Tetrahedron 164*, 134172. https://doi.org/10.1016/j.tet.2024.134172
10. Długosz, O., Szostak, K., Krupiński, M., & Banach, M. (2021). Synthesis of Fe_3O_4/ZnO nanoparticles and their application for the photodegradation of anionic and cationic dyes. *International Journal of Environmental Science and Technology*, *18*(3), 561–574. https://doi.org/10.1007/s13762-020-02852-4
11. Elviera, Yulizar, Y., Apriandanu, D. O. B., & Marcony Surya, R. (2022). Fabrication of novel $SnWO_4$/ZnO using Muntingia calabura L. leaf extract with enhanced photocatalytic methylene blue degradation under visible light irradiation. *Ceramics International*, *48*(3), 3564–3577. https://doi.org/10.1016/j.ceramint.2021.10.135
12. Gadore, V., Singh, A. K., Mishra, S. R., & Ahmaruzzaman, M. (2024). RSM approach for process optimization of the photodegradation of Congo red by a novel NiCo2S4/chitosan photocatalyst. *Scientific Reports*, *14*(1), 100886. https://doi.org/10.1038/s41598-024-51618-2
13. Gadow, S. I., Estrada, A. L., & Li, Y. Y. (2022). Characterization and potential of two different anaerobic mixed microflora for bioenergy recovery and decolorization of textile wastewater: Effect of C/N ratio, dye concentration and pH. *Bioresource Technology Reports*, *17*. https://doi.org/10.1016/j.biteb.2021.100886
14. Gaur, J., Vikrant, K., Kim, K. H., Kumar, S., Pal, M., Badru, R., Masand, S., & Momoh, J. (2023). Photocatalytic degradation of Congo red dye using zinc oxide nanoparticles prepared using Carica papaya leaf extract. *Materials Today Sustainability*, *22,* 100339. https://doi.org/10.1016/j.mtsust.2023.100339
15. Hariani, P. L., Rachmat, A., Hermansyah, & Yulianti, E. (2025). Synthesis of NiO-doped Fe_3O_4/chitosan-PVA composites for tetracycline degradation under visible light irradiation. *Ecological Engineering and Environmental Technology*, *26*(1), 292–304. https://doi.org/10.12912/27197050/196033
16. Hasanpour, M., Motahari, S., Jing, D., & Hatami, M. (2021). Statistical analysis and optimization of photodegradation efficiency of methyl orange from aqueous solution using cellulose/zinc oxide hybrid aerogel by response surface methodology (RSM). *Arabian Journal of Chemistry*, *14*(11), 103401. https://doi.org/10.1016/j.arabjc.2021.103401
17. Hemalatha, J., Senthil, M., Madhan, D., Al-Mohaimeed, A. M., & Al-onazi, W. A. (2024). Fabrication of $NiFe_2O_4$ nanoparticles loaded on activated carbon as novel composites for high efficient ultra violet-light photocatalysis for degradation of aqueous organic pollutants. *Diamond and Related Materials*, *144*, 110995. https://doi.org/10.1016/j.diamond.2024.110995
18. Hitkari, G., Chowdhary, P., Kumar, V., Singh, S., & Motghare, A. (2022). Potential of Copper-Zinc Oxide nanocomposite for photocatalytic degradation of Congo red dye. *Cleaner Chemical Engineering*, *1*, 100003. https://doi.org/10.1016/j.clce.2022.100003
19. Kannivelan, S., & Rajappan, K. (2025). Design and development of Ni MOF nanosheet-infused CA-modified PEI membrane for enhanced Congo red adsorption. *Inorganic Chemistry Communications*, *178*, 114550. https://doi.org/10.1016/j.inoche.2025.114550
20. Khan, A. A. P., Sonu, Sudhaik, A., Raizada, P., Khan, A., Rub, M. A., Azum, N., Alotaibi, M. M., Singh, P., & Asiri, A. M. (2023). AgI coupled SiO_2@$CuFe_2O_4$ novel photocatalytic nano-material for photo-degradation of organic dyes. *Catalysis Communications*, *179*, 106685. https://doi.org/10.1016/j.catcom.2023.106685
21. Khera, N., & Jeevanandam, P. (2025). Core-shell composite nanoarchitectonics of TiO_2@$NiCo_2S_4$ via thermal decomposition approach for photodegradation of Congo red. *Environmental Research*, *274*, 121304. https://doi.org/10.1016/j.envres.2025.121304
22. Kumar, E. V., Harini, R., Anitha, Kumara Swamy, B. E., & Nagaraju, G. (2025). One step facile green synthesis of $ZnFe_2O_4$-ZnO Nanocomposite: Efficient photocatalytic activity towards organic dyes under visible light and photoluminescence applications. *Environmental Nanotechnology, Monitoring and Management*, *23*, 101036. https://doi.org/10.1016/j.enmm.2024.101036

23. Liu, L., Chen, Z., Zhang, J., Shan, D., Wu, Y., Bai, L., & Wang, B. (2021). Treatment of industrial dye wastewater and pharmaceutical residue wastewater by advanced oxidation processes and its combination with nanocatalysts: A review. *Journal of Water Process Engineering, 42*, 102122. https://doi.org/10.1016/j.jwpe.2021.102122
24. Majeed, U., Alyousef, H. A., Alotaibi, B. M., Alrowaily, A. W., Al-Sehemi, A. G., & Saleem, M. I. (2024). Synthesis, physical and electrochemical characterization of $NiFe_2O_4$/ZnO nanocomposite for OER application. *Materials Chemistry and Physics*, *325*, 129682. https://doi.org/10.1016/j.matchemphys.2024.129682
25. Makofane, A., Maake, P. J., Mathipa, M. M., Matinise, N., Cummings, F. R., Motaung, D. E., & Hintsho-Mbita, N. C. (2022). Green synthesis of $NiFe_2O_4$ nanoparticles for the degradation of Methylene Blue, sulfisoxazole and bacterial strains. *Inorganic Chemistry Communications*, *139*, 109348. https://doi.org/10.1016/j.inoche.2022.109348
26. Malik, A. R., Aziz, M. H., Atif, M., Irshad, M. S., Ullah, H., Gia, T. N., Ahmed, H., Ahmad, S., & Botmart, T. (2022). Lime peel extract induced Ni-Fe2O4 NPs: Synthesis to applications and oxidative stress mechanism for anticancer, antibiotic activity. *Journal of Saudi Chemical Society*, *26*(2), 101422. https://doi.org/10.1016/j.jscs.2022.101422
27. Mohammadi, L., Khodadadi, Z., & Fazaeli, R. (2024). New insights into visible light active SnS semiconductor for the elimination of methylene blue: RSM and DFT approaches. *Materials Chemistry and Physics*, *313*, 128770. https://doi.org/10.1016/j.matchemphys.2023.12877
28. Mohan, N. S., Arulraj, A., Mangalaraja, R. V., Anitha, R., & Vijayalakshmi, V. (2024). Investigating the effect of nickel concentration on the photocatalytic activity of ZnO photocatalysts for methylene blue dye degradation prepared via facile green synthesis method. *Desalination and Water Treatment*, *320*, 100802. https://doi.org/10.1016/j.dwt.2024.100802
29. Muhaymin, A., Ahmad Mohamed, H. E., Hkiri, K., Safdar, A., Kotsedi, L., & Maaza, M. (2024). Green synthesis of $NiFe_2O_4$ nanoparticles using Hyphaene thebaica: A facile route towards magnetic and photocatalytic application. *Materials Today Chemistry*, *40*, 102286. https://doi.org/10.1016/j.mtchem.2024.102286
30. Panchakeaw, A., Nonthing, S., Dulyasucharit, R., & Nanan, S. (2025). Improved photocatalytic activity of magnetically separable Fe_3O_4/ZnO photocatalyst for complete sunlight-active removal of tetracycline antibiotic. *Chemical Physics Letters*, *862*, 141868. https://doi.org/10.1016/j.cplett.2025.141868
31. Pradhan, U. U., Karanam, A., M, R., & Krishna, R. (2025). Green synthesis of ZnO nanoparticles using Azadirachxta indica, Coffea arabica, Citrus sinensis and Mimosa pudica extracts: Characterization and photocatalytic degradation of methylene blue dye. *Materials Letters*, *397*, 138805. https://doi.org/10.1016/j.matlet.2025.138805
32. Rincón-Granados, K. L., Vázquez-Olmos, A. R., Rodríguez-Hernández, A. P., Vega-Jiménez, A., Ruiz, F., Garibay-Febles, V., & Ximénez-Fyvie, L. A. (2021). Facile solid-state synthesis and study in vitro of the antibacterial activity of NiO and $NiFe_2O_4$ nanoparticles. *Materialia*, *15*, 100955. https://doi.org/10.1016/j.mtla.2020.100955
33. Riyanti, F., Hasanudin, Rachmat, A., Muharni, Ibrahim, E., & Hariani, P. L. (2025). High-Performance Photocatalytic Degradation of Methylene Blue dye by NiO-integrated bentonite/Fe_3O_4. *International Journal of Environmental Science and Development*, *16*(4), 286–292. https://doi.org/10.18178/ijesd.2025.16.4.1536
34. Roy, N., Alex, S. A., Chandrasekaran, N., Kannabiran, K., & Mukherjee, A. (2022). Studies on the removal of acid violet 7 dye from aqueous solutions by green ZnO@Fe_3O_4 chitosan–alginate nanocomposite synthesized using Camellia sinensis extract. *Journal of Environmental Management*, *303*, 114128. https://doi.org/10.1016/j.jenvman.2021.114128
35. Saad, A. M., Abukhadra, M. R., Abdel-Kader Ahmed, S., Elzanaty, A. M., Mady, A. H., Betiha, M. A., Shim, J. J., & Rabie, A. M. (2020). Photocatalytic degradation of malachite green dye using chitosan supported ZnO and Ce–ZnO nano-flowers under visible light. *Journal of Environmental Management*, *258*, 110043. https://doi.org/10.1016/j.jenvman.2019.110043
36. Sarani, M., Bazookar Joshaghani, A., Najafidoust, A., Abbasi Asl, E., Kazemi Hakki, H., Bananifard, H., & Sillanpaa, M. (2021). Sun-light driven photo degradation of organic dyes from wastewater on precipitation Ag_2CrO_4 over SiO_2-aerogel and nano silica. *Inorganic Chemistry Communications*, *133*, 108877. https://doi.org/10.1016/j.inoche.2021.108877
37. Sarkar, C., Basu, J. K., & Samanta, A. N. (2021). Synthesis of novel ZnO/Geopolymer nanocomposite photocatalyst for degradation of Congo red dye under visible light. *Environmental Nanotechnology, Monitoring and Management*, *16*, 100521. https://doi.org/10.1016/j.enmm.2021.100521
38. Sharma, Y., Anand, V., Kumar, R., Kumar, A., & Heera, P. (2025). Green synthesized ZnO nanoparticles using Jatropha curcas latex for antibacterial applications. *Next Materials*, *8*, 100869. https://doi.org/10.1016/j.nxmate.2025.100869
39. Shokri, S., Shariatifar, N., Molaee-Aghaee, E., Khaniki, G. J., Sadighara, P., Faramarzi, M. A., Mohammadi,

M., & Rezagholizade-shirvan, A. (2023). Synthesis and characterization of a novel magnetic chitosan–nickel ferrite nanocomposite for antibacterial and antioxidant properties. *Scientific Reports*, *13*(1), 15777. https://doi.org/10.1038/s41598-023-42974-6

40. Sofia, G., Koventhan, C., Kanmani, S., & Lo, A. Y. (2025). Green synthesized rGO/TiO_2/g-C_3N_4 nanocomposites via Plectranthus amboinicus extract for efficient photocatalytic degradation of methylene blue: RSM optimization, antimicrobial and phytotoxicity assessment. *Journal of Environmental Chemical Engineering*, *13*(1), 115267. https://doi.org/10.1016/j.jece.2024.115267
41. Taslim, N. A., Sutisna, N., Nurkolis, F., Qhabibi, F. R., Kurniawan, R., & Mayulu, N. (2023). Dietary supplementation of Muntingia calabura leaves ameliorates reactive oxygen species and malondialdehyde levels: clinical study on alloxan-induced hyperglycemic rats. *Clinical Nutrition Open Science*, *48*, 87–96. https://doi.org/10.1016/j.nutos.2023.03.004
42. Thirumavalavan, M., Sukumar, K., & Sabarimuthu, S. Q. (2024). Trends in green synthesis, pharmaceutical and medical applications of nano ZnO: A review. In *Inorganic Chemistry Communications, 169*, 113002. https://doi.org/10.1016/j.inoche.2024.113002
43. Tijani, J. O., Daniel, A. I., Onogwu, S. U., Abdulkareem, A. S., Aminu, U. A., Keyster, M., & Klein, A. (2025). Effects of ZnO nanoparticles concentration on the morphology and textural properties of ZnO/$NiFe_2O_4$ nanocomposite. *MethodsX*, *14*, 103199. https://doi.org/10.1016/j.mex.2025.103199
44. Tripta, & Rana, P. S. (2023). $NiFe_2O_4$/ZnO nanocomposites for degradation of MB dye with their local electrical behavior. *Journal of Molecular Structure*, *1282*, 135160. https://doi.org/10.1016/j.molstruc.2023.135160
45. Winiarska, K., Klimek-Ochab, M., Wilk, Ł. J., & Winiarski, J. (2025). Green synthesis of ZnO nanoparticles using spent coffee extract: Comprehensive characterization and insights. *Materials Chemistry and Physics*, *338*, 130621. https://doi.org/10.1016/j.matchemphys.2025.130621
46. Yizengaw, D. E., Godie, E. M., & Manayia, A. H. (2025). Green synthesis and characterization of ZnO nanoparticles using Justicia Schemperiana leaf extract and its antibacterial and antioxidant activity. *Inorganic Chemistry Communications*, *174*, 114071. https://doi.org/10.1016/j.inoche.2025.114071
47. Zhang, X., Li, Y., Li, M., Zheng, H., Du, Q., Li, H., Wang, Y., Wang, D., Wang, C., Sui, K., Li, H., & Xia, Y. (2019). Preparation of improved gluten material and its adsorption behavior for Congo red from aqueous solution. *Journal of Colloid and Interface Science*, *556*, 249–257. https://doi.org/10.1016/j.jcis.2019.08.037